# Clues to the Electrical Switching Mechanism of Carbazole-Containing Polyimide Thin Films

Brian J. Ree,[†] Wonsang Kwon,[†] Kyungtae Kim,[†] Yong-Gi Ko, Young Yong Kim, Hoyeol Lee, and Moonhor Ree*

Department of Chemistry, Division of Advanced Materials Science, Center for Electro-Photo Behaviors in Advanced Molecular Systems, Pohang Accelerator Laboratory, Polymer Research Institute, and BK School of Molecular Science, Pohang University of Science & Technology (POSTECH), Pohang 790-784, Republic of Korea

ABSTRACT: The mechanism behind electrical memory behavior of carbazole-containing polyimides (PIs) in nanoscale thin films was investigated. For this investigation, a series of poly(3,3′-dihydroxy-4,4′-biphenylene-*co*-3,3′-bis(*N*-ethyleny-loxycarbazole)-4,4′-biphenylene hexafluoro-isopropylidenediphthalimide)s (6F-HAB-HABCZ$_n$ PIs) with various compositions was synthesized as a model carbazole-containing polymer system. The thermal properties, band gaps, and molecular orbital levels of the PIs were determined. Furthermore, the chemical compositions, as well as the nanoscale thin film morphologies and electron densities, were analyzed, providing detailed information on the population and positional distribution of carbazole moieties in thin films of the PIs. PI Devices were fabricated with aluminum electrodes and tested electrically. The PI thin film layers in the devices exhibited electrically permanent memory behavior, which was driven by trap-limited space-charge limited conduction and ohmic conduction. The permanent memory characteristics were found to be attributed to the incorporated carbazole moieties rather than from the other chemical components. Furthermore, the memory characteristics depended significantly on the population and positional distribution of carbazole moieties in the PI layer, as well as the film thickness. Considering that the backbone is not conjugated, the present results collectively indicate that the electrical switching behavior of the PI films is driven by the carbazole moieties acting as charge traps and a hopping process using the carbazole charge-trap sites as stepping-stones.

KEYWORDS: *carbazole-containing polyimide, digital memory device, nonvolatile memory characteristics, memory mechanism, carbazole population dependency, carbazole distribution denpendency, film thickness dependency, charge-trap, charge hoping process*
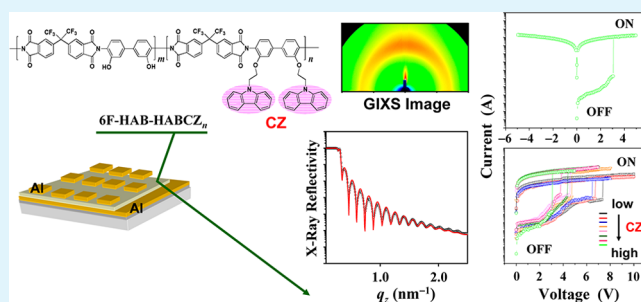
INTRODUCTION

In general, organic polymers can be easily tailored their properties through chemical synthesis. They can be further easily processed with miniaturized dimensions as well as in multistack layer structures. Because these characteristics, much attention has been devoted to developing electrical memory polymers that can be an alternative of silicon- and metal-oxide-based memory materials.[1−4] The efforts have resulted in the development of several electrical memory polymer systems.[1−4]

In particular, a few memory polymer systems based on thermally stable polyimides containing carbazole units were reported so far.[5−10] Several switching mechanisms have been proposed to explain the electrical memory behavior in these systems: ohmic conduction, Schottky conduction, thermionic conduction, space charge-limited conduction (SCLC), Frenkel-Poole conduction, tunneling conduction, ionic conduction, polymer fuse conduction, hopping conduction, charge-transfer conduction, conformation change conduction, and so on.[2−4] The majority of these mechanisms was proposed to interpret the current−voltage behavior of devices. Nevertheless, the exact mechanisms underlying the electrical memory behavior of polymer films have yet to be investigated in detail. In fact, the

switching mechanism in electrical memory polymer films may be complicate because their chemical composition, molecular structure, morphological structure, and properties are integrated together into a device with metal electrodes, producing electrical memory performance. A variety of factors may affect the electrical switching behavior of polymer films, including π-conjugation, non-π-conjugation, charge-trapping sites, molecular orbital levels, band gap, charge-trap power, charge-trap capacity, trapped-charge stabilization power, trapped-charge releasing ability, population of charge-trap sites, geometrical distribution of charge-trap sites, film thickness, charge mobility, electrode work function, interfacial contact, electric field strength, and voltage sweep direction. Therefore, a detailed investigation is needed to understand the switching mechanisms in such films.

In this report, we synthesized poly(3,3′-dihydroxy-4,4′-biphenylene-*co*-3,3′-bis(*N*-ethylenyloxycarbazole)-4,4′-biphenylene hexafluoroisopropylidenediphthalimide)s (6F-HAB-

Scheme 1. Syntheses of 6F-HAB-HABCZ_n PIs
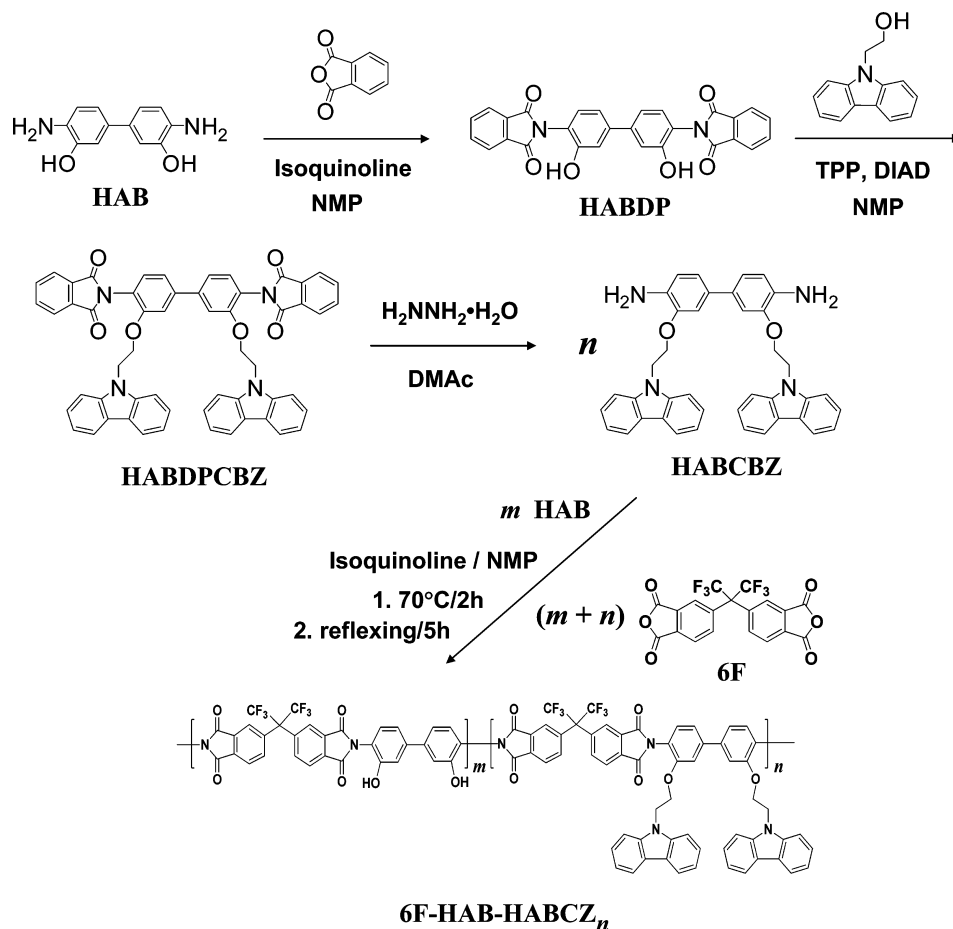
HABCZ_n PIs) with various compositions as a model carbazole-containing polymer system and investigated their electrical memory mechanism. The chemical compositions of the synthesized PIs were characterized by proton nuclear magnetic resonance (^{1}H NMR) spectroscopy. Nanoscale thin film morphologies of the PIs were examined by synchrotron grazing incidence X-ray scattering (GIXS) and X-ray reflectivity (XR) analysis. Their devices with aluminum electrodes exhibited electrically permanent memory behavior. The nonvolatile memory performance was found to be associated with the presence of carbazole moieties rather than the other chemical components and, further, to significantly depend on the population and geometrical distributions of carbazole moieties as well as on the film thickness. Collectively, the present findings indicate that the electrical switching behaviors of the polymer films are driven by the carbazole moieties acting as charge traps and a hopping process in which the carbazole charge-trap sites are used as stepping-stones.

■ EXPERIMENTAL SECTION

Materials. 2,2′-Bis(3,4-dicarboxyphenyl)hexafluoropropane dianhydride (6F) was obtained from Chriskev (Lenexa, KS, USA) and then purified by recrystallization in acetic anhydride just before use.[11] 3,3′-Dihydroxy-4,4′-diaminobiphenyl (HAB) was also purchased from Chriskev and dried at 100 °C under vacuum for 1 day just before use.[11] All other chemicals were purchased from Aldrich (St. Paul, MN, USA). N-Methyl-2-pyrrolidone (NMP) and N-dimethylacetamide (DMAc) were distilled over calcium hydride under reduced pressure

and over calcium sulfate under reduced pressure before use, respectively. All other chemicals were used as received.

Synthesis. 6F-HAB-HABCZ_n PIs have been synthesized in a four stages (Scheme 1), according a method reported in the literature.[5,11,12] In the first stage, 3,3′-dihydroxy-4,4′-(diphthalimido)biphenyl (HABDP) was synthesized in anhydrous NMP containing isoquinoline from HAB and phthalic anhydride; the reaction was carried out at 170 °C for 2 h. The target product HABDP was obtained with 96% yield. In the second stage, HABDP was reacted with 9H-carbazole-9-ethanol in anhydrous NMP under the aids of triphenylphosphine (TPP) and diisopropyl azodicarboxylate (DIAD), producing 3,3′-bis[9-carbazole(ethyloxy)]-4,4′-(diphthalimido)biphenyl (HABDPCZ) in a yield of 78%. In the third stage, HABDPCZ was further converted to 3,3′-bis[9-carbazole(ethyloxy)biphenyl]-4,4′-diamine (HABCZ); the yield was 64%. In the final stage, 6F-HAB-HABCZ_n PI was synthesized in various compositions by the polycondensation reaction and subsequent imide-ring-closure reaction of 6F with HAB and HABCZ in anhydrous NMP containing isoquinoline. A typical polymerization procedure was as follows. 6F (6F, 6.00 g, 13.5 mmol), HABCZ (5.7 g, 9.45 mmol) and HAB (0.876 g, 4.05 mmol) were dissolved in anhydrous NMP (125 mL) containing isoquinoline catalyst (3.2 mL, 27.0 mmol). The polycondensation reaction was conducted at room temperature for 3 h under stirring. Then the imide-ring-closure reaction was performed at 70 °C for 2 h under continuous stirring and subsequently refluxed for 5 h. The PI product was obtained with 98% yield after purification. In the same manner, the other 6F-HAB-HABCZ_n PIs were synthesized. The product in each reaction was confirmed by proton carbon probes nuclear magnetic resonance (^{1}H and ^{13}C NMR) spectroscopy (model AV300 FT-NMR, Bruker, Rheinstetten, Gemany); deuterated dimethyl sulfoxide (DMSO-d_6) and tetramethylsilane were used as a solvent and an internal standard, respectively.

The obtained 6F-HAB-HABCZ$_n$ PIs were soluble in cyclopentanone, giving homogeneous solutions. The PI solutions were found to provide high quality films via a common spin-cast process. For both thin film analysis and device fabrication, homogeneous 6F-HAB-HABCZ$_n$ PI solutions (1.0 wt %) were prepared in cyclopentanone and then filtered using polytetrafluoroethylene-membrane-based (PTFE) micro filters (0.20 μm pore size). The spin-cast PI films were dried at 80 °C for 8 h in vacuo. Their thicknesses were measured by using a spectroscopic ellipsometer (model M2000, Woollam, Lincoln, NE, USA) or an alpha-stepper (Vecco Instruments, Santa Clara, CA, USA).

Measurements. Thermal properties of the synthesized polymers were characterized by thermogravimetry (TGA) and differential scanning calorimetry (DSC) using a Seiko thermal analysis system (model TG/DTA-6300 and model DSC 220CU, Tokyo, Japan). TGA runs were performed over the temperature range 25 to 700 °C under nitrogen atmosphere. DSC runs were carried out over the range −50 to 300 °C under nitrogen atmosphere. A ramping rate of 10.0 °C/min was employed.

Ultraviolet−visible (UV−vis) spectra were measured using a spectrometer (model S-3100, Scinco, Seoul, Korea). Here, the PI films coated onto quartz glasses were used. The band gap of a PI film sample was estimated from the absorption edge in the measured UV−vis spectrum.

Cyclic voltammetry (CV) was carried out with a scan rate of 100 mV/s on an electrochemical workstation (IM6ex impedance analyzer) equipped with a three-electrode cell; the cell consisted of a counter electrode (platinum gauze), a reference electrode(Ag/AgCl (saturated KCl)), and a gold (Au) electrode deposited on silicon wafer (which was coated with PI). The external ferrocene/ferrocenium (F_c/F_c^+) redox standard $E_{1/2}$ was measured to be 0.40 V vs Ag/AgCl in acetonitrile. The highest occupied molecular orbital (HOMO) level for the F_c/F_{c+} standard was assumed to be −4.80 eV with respect to the zero vacuum level.

Grazing incidence X-ray scattering (GIXS) analysis was carried out with an incident angle α_i of 0.160° at the 3C beamline of the Pohang Light Source Facility, according to the method reported previously.[13−15] An X-ray radiation source (0.1129 nm wavelength λ) and a two-dimensional (2D) charge-coupled detector (CCD, MAR USA, Evanston, IL, USA) were used. The sample-to-detector distances were 230.7, 928.4, and 2922.7 mm. All scattering measurements were performed at room temperature; the data collection time in each measurement was 30−60 s. Scattering angles were corrected with respect to the reflected X-ray beam and the scattering data of a precalibrated silver behenate (TCI, Tokyo, Japan) powder.

XR analysis was further conducted with an X-ray beam (λ = 0.1541 nm) in θ−2θ scanning mode at the 3D beamline[16,17] of the Pohang Light Source Facility using a Huber four-circle goniometer equipped with a scintillation counter (model EDR, Bede Scientific, Centennial, CO, USA). In measurements the reflected beam intensity was normalized by the primary beam intensity that was measured using an ionization chamber.

Simple PI devices with two electrodes were fabricated. Silicon (Si) wafers with native oxide layer were used as substrates. Nanoscale thin films of the PIs were prepared by spin-cast and subsequent drying at 80 °C for 8 h in vacuo; PI solutions in cyclopentanone (1.0 wt % PI) were used. Thin aluminum (Al) film (300 nm thick) was deposited onto Si substrates as a bottom electrode by electron-beam sputtering. Al top electrodes (300 nm thick) were prepared with sizes between 0.5 × 0.5 and 2.0 × 2.0 mm^2 onto the PI film layers through a shadow mask by means of thermal evaporation. Current−voltage (I−V) analysis was conducted with a scan rate of 500 mV/s in air ambient using a semiconductor analyzer (model 4200-SCS, Keithley, Cleveland, OH, USA).

■ RESULTS AND DISCUSSION

A series of 6F-HAB-HABCZ$_n$ PIs with various compositions was synthesized. The chemical compositions were determined by ^{1}H NMR spectroscopy (Figure 1). For each PI, the portion
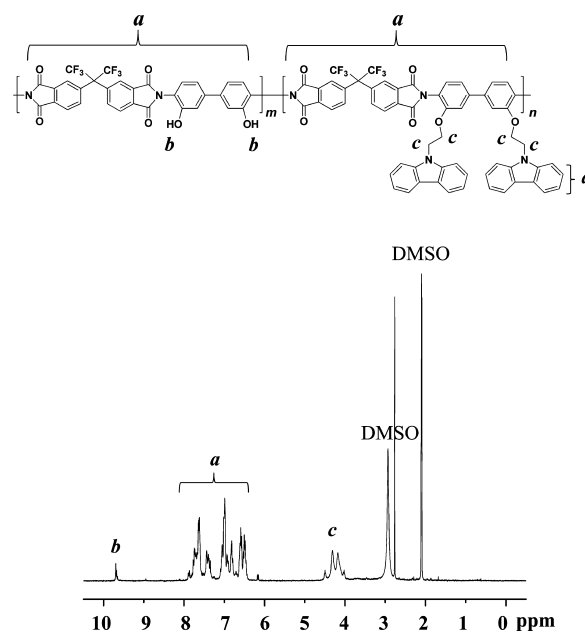

Figure 1. ^{1}H NMR spectrum of 6F-HAB-HABCBZ$_{80.6}$ PI in DMSO-d_6.

of the HABCZ unit (i.e., carbazole moiety) was determined by the integrating the Ar−OH proton peak (9.7 ppm) arising from the HAB unit and the OCH$_2$CH$_2$ proton peaks (4.5−4.0) generated by both the HAB and HABCZ units. The chemical compositions obtained are summarized in Table 1.

All of the PIs showed good solubility in cyclopentanone, giving homogeneous solutions. In addition, they produced high-quality films through a simple common spin-coating process. The 6F-HAB-HABCZ$_{100}$ PI (i.e., 6F-HABCZ PI) was found to start the glass transition at 225 °C (= T_g, glass transition temperature) and degradation at 325 °C (= T_d, degradation temperature). The 6F-HAB-HABCZ$_0$ PI (i.e., 6F-HAB PI) had a T_d of 368 °C; this PI showed no glass transition below 300 °C. The PIs with other compositions revealed intermediate T_g and T_d values between those of 6F-HAB-HABCZ$_{100}$ and 6F-HAB-HABCZ$_0$ PI. In addition, the 6F-HAB-HABCZ$_{100}$ PI exhibited a HOMO level (E_{HOMO}) of −5.71 eV and a LUMO level (E_{LUMO}) of −2.23 eV, which were measured from UV−vis spectroscopy and CV analysis. These E_{HOMO} and E_{LUMO} values result mainly from the carbazole moieties incorporated as side groups. Thus, the other PIs bearing carbazole moieties showed similar E_{HOMO} and E_{LUMO} values.

The nanoscale thin film morphologies of 6F-HAB-HABCZ$_n$ PIs were investigated by means of synchrotron grazing incidence wide and small angle scattering (GIWAXS and GISAXS) analysis (Figure 2A). Figure 2B−E depict representatives of the 2D GIWAXS patterns measured for the PI thin films (30−55 nm thick). The out-of-plane and in-plane scattering profiles (which were extracted from the 2D scattering patterns) are displayed in Figure 2F, G, respectively. All PI films revealed two broad weak scattering rings, one centered around 11° (the first ring peak) and another centered around 14.5° (the second ring peak), which are most likely amorphous halos. For each film, the first ring peak had a much higher intensity than the second ring peak, and the wide angle tail of the first peak overlapped heavily with the second peak. Moreover, both of the scattering rings are anisotropic in intensity toward the meridian line, rather than isotropic. Considering the

Table 1. Structural Parameters of 6F-HAB-HABCZ$_n$ PI Thin Films Determined by GIWAXS Analysis

PI film	n_{HABCZ}^a (mol %)	first peak[b]		second peak[c]		R^f	$\bar{\varphi}^g$ (deg)	σ_φ^h (deg)	O_s^i
		$d_{1,\perp}^d$ (nm)	$d_{1,\parallel}^e$ (nm)	$d_{2,\perp}^d$ (nm)	$d_{2,\parallel}^e$ (nm)				
6F-HAB-HABCz$_0$	0.0	0.560 (0.002)^j	0.581 (0.002)	0.423 (0.002)	0.453 (0.002)	1.17	0	76.71	0.265
6F-HAB-HABCz$_{0.8}$	0.8	0.549 (0.002)	0.568 (0.003)	0.425 (0.002)	0.453 (0.002)	1.15	0	74.56	0.274
6F-HAB-HABCz$_{1.9}$	1.9	0.553 (0.002)	0.573 (0.002)	0.426 (0.002)	0.454 (0.002)	1.16	0	73.56	0.278
6F-HAB-HABCz$_{2.9}$	2.9	0.554 (0.002)	0.574 (0.002)	0.430 (0.002)	0.454 (0.002)	1.13	0	73.23	0.279
6F-HAB-HABCz$_{5.3}$	5.3	0.557 (0.002)	0.576 (0.002)	0.433 (0.002)	0.454 (0.002)	1.19	0	72.98	0.280
6F-HAB-HABCz$_{6.9}$	6.9	0.558 (0.002)	0.576 (0.002)	0.433 (0.002)	0.456 (0.002)	1.17	0	72.67	0.282
6F-HAB-HABCz$_{12.0}$	12.0	0.560 (0.002)	0.578 (0.003)	0.433 (0.002)	0.456 (0.002)	1.17	0	72.14	0.284
6F-HAB-HABCz$_{24.6}$	24.6	0.562 (0.002)	0.580 (0.002)	0.434 (0.002)	0.457 (0.002)	1.15	0	71.99	0.285
6F-HAB-HABCz$_{27.0}$	27.0	0.562 (0.002)	0.583 (0.002)	0.435 (0.002)	0.457 (0.002)	1.16	0	71.66	0.287
6F-HAB-HABCz$_{56.0}$	56.0	0.565 (0.002)	0.585 (0.002)	0.437 (0.002)	0.458 (0.002)	1.19	0	71.09	0.289
6F-HAB-HABCz$_{80.6}$	80.6	0.566 (0.002)	0.591 (0.002)	0.439 (0.002)	0.459 (0.002)	1.14	0	70.66	0.291
6F-HAB-HABCz$_{100}$	100.0	0.567 (0.002)	0.592 (0.002)	0.440 (0.002)	0.461 (0.002)	1.17	0	70.04	0.294

^{a}The mol % of HABCZ unit in 6F-HAB-HABCZ$_n$, which was determined by ^{1}H NMR spectroscopy. ^{b}The scattering peak centered around 11°. ^{c}The scattering peak centered around 14.5°. ^{d}The d-spacing of the scattering peak along the α_f direction (i.e., out-of-plane direction). ^{e}The d-spacing of the scattering peak along the $2\theta_f$ direction (i.e., in-plane direction). $^fR = I_{max,\mu=0°}/I_{max,\mu=\pm90°}$ where $I_{max,\mu=0°}$ is the intensity at the peak maximum in the azimuthal scattering profile of the peak 1, which corresponds to the intensity at an azimuthal angle μ of 0°, and $I_{max,\mu=\pm90°}$ is the intensity at the peak minimum in the azimuthal scattering profile of the peak 1, which corresponds to the intensity at an azimuthal angle μ of $\pm90°$ (Figure 2H). ^{g}The mean orientation angle; here the orientation angle φ is defined by the polar angle between the orientation vector $\mathbf{n}$ and the out-of-plane of the film where the vector $\mathbf{n}$ is given for the normal direction of PI chain with respect to the out-of-plane of the film. ^{h}The standard deviation of orientation angle φ from $\bar{\varphi}$. ^{i}Second-order orientation factor. ^{j}Error bar, which was extracted over the sweep range $\pm1.0\%$ of the χ^2 value obtained by best-fitting the GIXS data with a Gaussian function: $\chi^2 = \sum(\log_{10}x_o^i - \log_{10}x_c^i)^2$ where x_o^i and x_c^i are the ith measured and calculated data, respectively. Thus, this error bar is different from common standard deviation. Fitting of the scattering data with a Gaussian function was carried out with good statistics and analysis quality was checked by χ^2 and Ω (%) values, where Ω (%) $= 100(\chi^2/\sum(\log_{10}x_c^i)^2)^{1/2}$. The quality of the scattering data analysis was achieved with $\Omega = 0.3-1.0\%$.

amorphous halo characteristics and the chemical structure of the PIs, the first scattering peak likely originates from the average interdistance of the PI chains while the second peak can be attributed to the average interdistance between the side groups and/or the backbone and the side groups. Depending on the chemical composition (i.e., the carbazole moiety content), the first scattering peak was determined to have a d-spacing of 0.549−0.567 nm ($= d_{1,\perp}$) in the out-of-plane direction and of 0.568−0.592 nm ($= d_{1,\parallel}$) in the in-plane direction (Figure 3A; Table 1). The d-spacing of the second peak varied in the range 0.425−0.440 nm ($= d_{2,\perp}$) along the out-of-plane direction and 0.453−0.461 nm ($= d_{2,\parallel}$) in the in-plane direction (Figure 3B; Table 1). Overall, both the d_1 and d_2 values increased with increasing carbazole moiety content in the PI polymer, which can be attributed to the bulkiness of the carbazole moiety. Furthermore, the $d_{1,\perp}$ and $d_{2,\perp}$ values were relatively smaller than the $d_{1,\parallel}$ and $d_{2,\parallel}$ values, respectively, indicating that the PI molecules in the thin films were more densely packed in the out-of-plane direction than in the in-plane direction. This anisotropic molecular packing originated from the preferential in-plane orientation of the PI chains in the nanoscale thin films on silicon substrates.

To get more information about the orientation of the PI chains in the thin films, an azimuthal profile was extracted from the first scattering peak in each 2D GIXS pattern and then followed by analysis. The azimuthal scattering intensity $I_{GIXS,\varphi}(\mu)$ can be generally obtained by integrating $I_{GIXS}(\mu)$ over possible orientations of the PI chain:[18]

$$I_{GIXS,\varphi}(\mu) = \int_{-\pi}^{\pi} I_{GIXS}(\mu)D(\varphi)d\varphi \tag{1}$$

where $D(\varphi)$ is a distribution function of the orientation vector $\mathbf{n}$ for the normal direction of the PI chain with respect to a direction perpendicular to the film plane; φ is the polar angle between the $\mathbf{n}$ vector and the direction perpendicular to the

film plane. The second order orientation factor O_s, a measure of the orientation of the PI chain, can be defined as the following equation[18]

$$O_s = \int D(\varphi)\frac{(3\cos^2\varphi - 1)}{2}d\varphi \tag{2}$$

As shown in Figure 2H, all the azimuthal scattering profiles were successfully well-fitted by using eq 1 with a Gaussian distribution function

$$D(\varphi) = \frac{1}{\sqrt{2\pi}\,\sigma_\varphi}\exp\left[-\frac{(\varphi - \bar{\varphi})^2}{2\sigma_\varphi^2}\right] \tag{3}$$

where $\bar{\varphi}$ and σ_φ are the average angle and standard deviation of φ from $\bar{\varphi}$, respectively. These orientation analysis results are summarized in Table 1 and Figure 3C.

For all of the PI films, $\bar{\varphi} = 0$. As the carbazole moiety content increased, however, the σ_φ value decreased from 76.71° to 70.04°. As a result, the O_s value increased from 0.265 to 0.294. The ratio of the maximum peak intensity at $\mu = 0°$ and the minimum peak intensity at $\mu = \pm 90°$ (i.e., $R = I_{max,\mu=0°}/I_{max,\mu=\pm90°}$) varied in the range 1.13−1.19. These results collectively inform that the PI chains in the nanoscale thin films were somewhat preferentially oriented along the film plane; however, their orientation was very broad in angle distribution. The degree of in-plane orientation was slightly enhanced with increasing carbazole moiety content in the PI polymer. In addition, grazing incidence small-angle X-ray scattering (GISAXS) measurements were conducted on the PI films. All of the films showed featureless scattering patterns (data not shown), suggesting that no nanostructure had developed in the PI films.

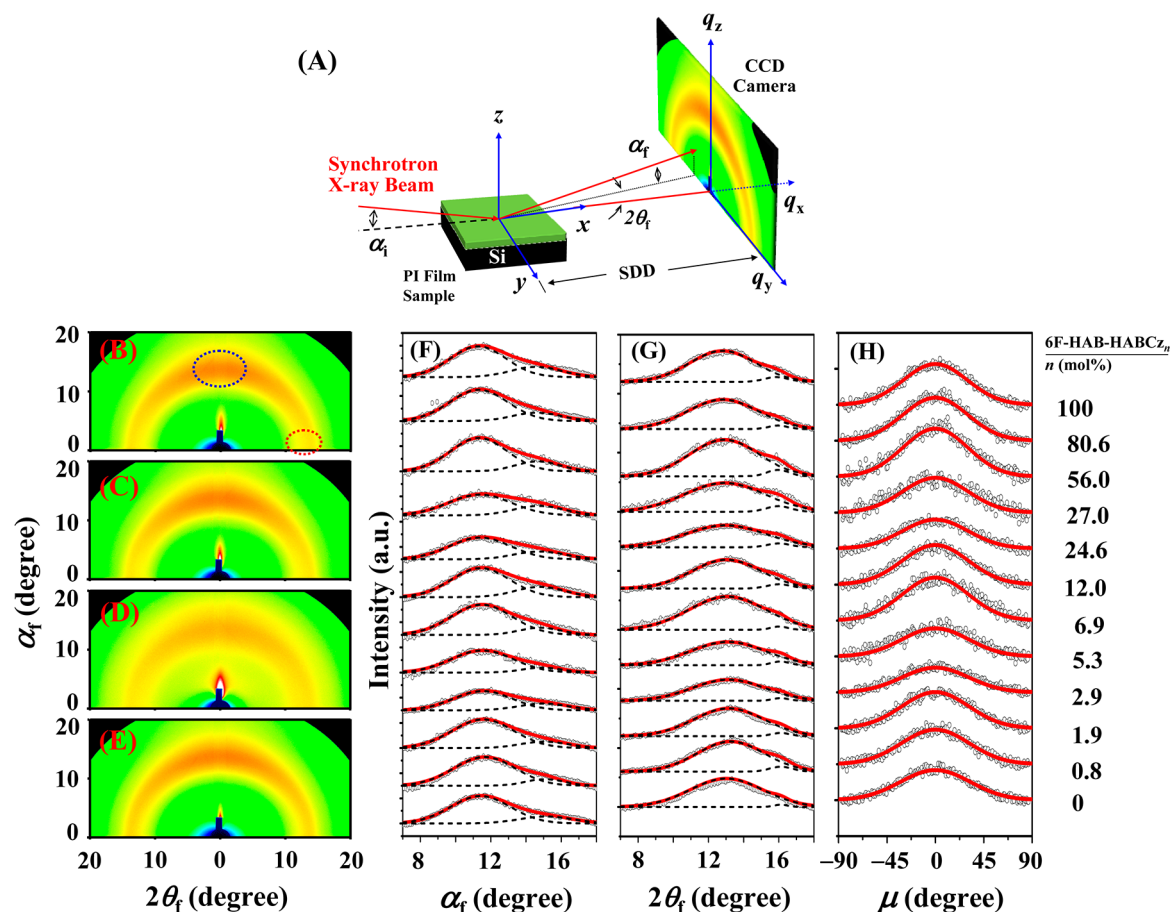The PI films were further investigated by synchrotron XR analysis. As depicted in Figure 4, the measured XR data could

Figure 2. (A) Geometry of GIXS: α_i is the incident angle at which the X-ray beam impinges on the film surface; α_f and $2\theta_f$ are the exit angles of the X-ray beam with respect to the film surface and to the plane of incidence respectively; and q_x, q_y, and q_z are the components of the scattering vector **q**. Representative synchrotron GIWAXS patterns of the PI films (30−55 nm thick) coated onto silicon substrates, which were measured at $\alpha_i =$ 0.160° using an X-ray beam with a wavelength λ of 0.1129 nm; (B) 6F-HAB-HABCBZ$_{100}$ PI; (C) 6F-HAB-HABCBZ$_{80.6}$ PI; (D) 6F-HAB-HABCBZ$_{27.0}$ PI; (E) 6F-HAB-HABCBZ$_0$ PI; (F) out-of-plane scattering profiles extracted from the 2D scattering patterns including the data in B−E along the α_f direction at $2\theta_f = 0.370°$; (G) in-plane scattering profiles extracted from the 2D scattering patterns along the $2\theta_f$ direction at $\alpha_f = 0°$; (H) azimuthal scattering profiles of the scattering peak at 14.000°, which were extracted from the 2D scattering patterns. In F and H, the black symbols are the measured data, the solid lines were obtained by fitting the data using a Gaussian function, and the dashed lines were obtained by deconvolution of the data.

be well fitted using Parratt's fitting algorithm.[17,19] This XR analysis found that the electron density (ρ_e) value varies in the range 357.9−461.3 nm^{-3} depending on the carbazole moiety content, with higher carbazole contents producing lower electron densities in the PI film (Table 1).

Taking into consideration the thin film morphological characteristics described above, devices were fabricated with an active PI film layer (20 nm thick) and metal electrodes (Figure 5A) and tested electrically. The 20 nm-thick 6F-HAB-HABCZ$_{100}$ PI film initially exhibited a high-resistance state (i.e., the OFF-state) (Figure 5B). When a positive voltage was applied with a current compliance of 0.01 A, the current was, however, abruptly increased at around +3.0 V (which corresponds to the critical voltage $V_{c,ON}$ to switch on the device) (Figure 5B). Thus, this device underwent a sharp electrical transition from the OFF-state to the ON-state. Once the device was in the ON-state, it remained in that state, regardless of the elimination of electrical power or any further reverse and forward voltage sweeps. Overall, the 6F-HAB-HABCZ$_{100}$ device exhibited write-once-read-many-times (WORM) memory behavior. Similar WORM memory behavior was observed for 20 nm-thick films of the other PIs with

carbazole content ≥5.3 mol % (Figure 5C). However, as the carbazole content was decreased to 5.3 mol %, the $V_{c,ON}$ value increased and the current level at the ON-state became lower (Figure 5C; Table 2). Surprisingly, the PI films with carbazole content ≤2.9 mol % exhibited dielectric characteristics rather than memory characteristics (Figure 5D).

For the PIs with carbazole content ≤2.9 mol %, additional devices were fabricated with thinner films. Figures 5E and 5F show representative I−V data of the devices fabricated with PI films of 12 nm thick. In contrast to the dielectric characteristics observed for the 20 nm thick films, the devices with 12 nm thick films exhibited WORM memory behaviors. The $V_{c,ON}$ value was also further increased with decreasing the carbazole content in the PI polymer (Figure 5F; Table 2). In contrast, none of the devices fabricated with 6F-HAB-HABCZ$_0$ (i.e., the PI containing no carbazole) exhibited memory behavior (Figure 5G).

The I−V data measured above were further analyzed with various conduction models[2,5,20] in order to get information on the electrical switching mechanisms. These analyses found that the I−V data of the OFF state could be fitted well with a trap-limited space-charge limited conduction (SCLC) model could
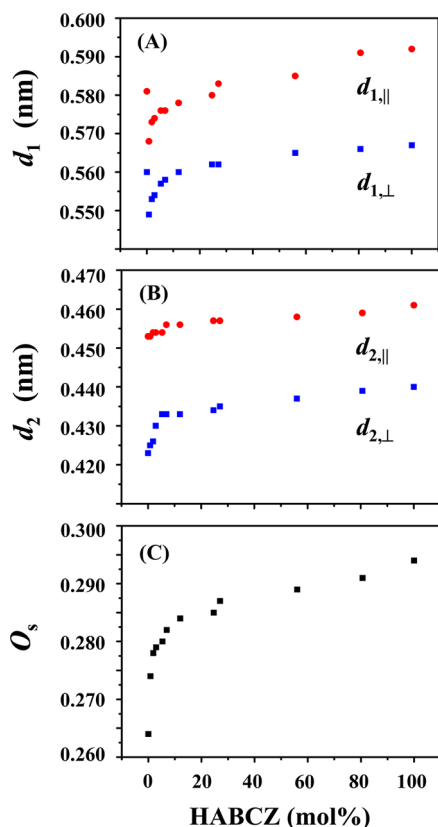
Figure 3. Variations in the thin film structural parameters with the HABCZ content, which were determined from the GIWAXS data in Figure 3: (A) d-spacing of the scattering peak 1; (B) d-spacing of the scattering peak 2; (C) orientation factor of the PI chains.
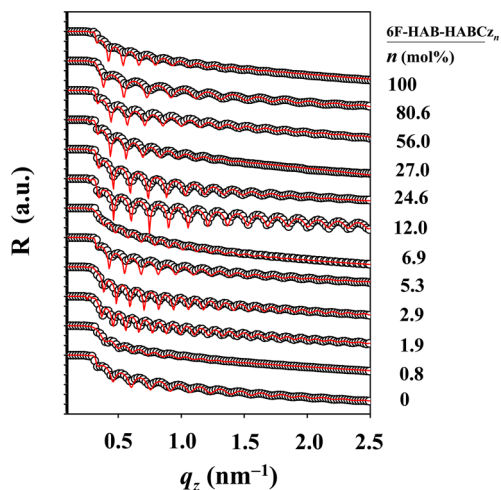

Figure 4. Representative XR profiles of the PI films (30−55 nm thick) coated onto silicon substrates. The wavelength λ of the X-ray beam was 0.1541 nm. The symbols are the measured data and the solid lines are the curves fitted to the data.

Figure 5. Typical $I-V$ curves of (A) the Al/PI/Al devices, which were measured with a compliance current set of 0.01 A: (B) 20 nm thick 6F-HAB-HABCBZ$_{100}$ PI film; (C) 20 nm thick 6F-HAB-HABCBZ$_n$ PI films (n = 5.3, 6.9, 12.0, 24.6, 27.0, 56.0, 80.6, and 100.0 mol %); (D) 20 nm thick 6F-HAB-HABCBZ$_n$ PI films (n = 0.0, 0.8, 1.9, and 2.9 mol %); (E) 12 nm thick 6F-HAB-HABCBZ$_{2.9}$ PI film; (F) 12 nm thick 6F-HAB-HABCBZ$_n$ PI films (n = 0.8, 1.9, and 2.9 mol %); (G) 6F-HAB-HABCBZ$_0$ PI films (5 and 10 nm thick). The electrode contact area was 0.5×0.5 mm^2.

(Figure 6A−C), whereas those of the ON state could be successfully fitted with an ohmic contact model (Figure 6D). Collectively these results inform that the devices in the OFF state were mainly governed by a trap-limited SCLC mechanism whereas those in the ON state were predominantly operated by an ohmic conduction mechanism. Considering the HOMO and LUMO levels of the PIs and the work function of the Al
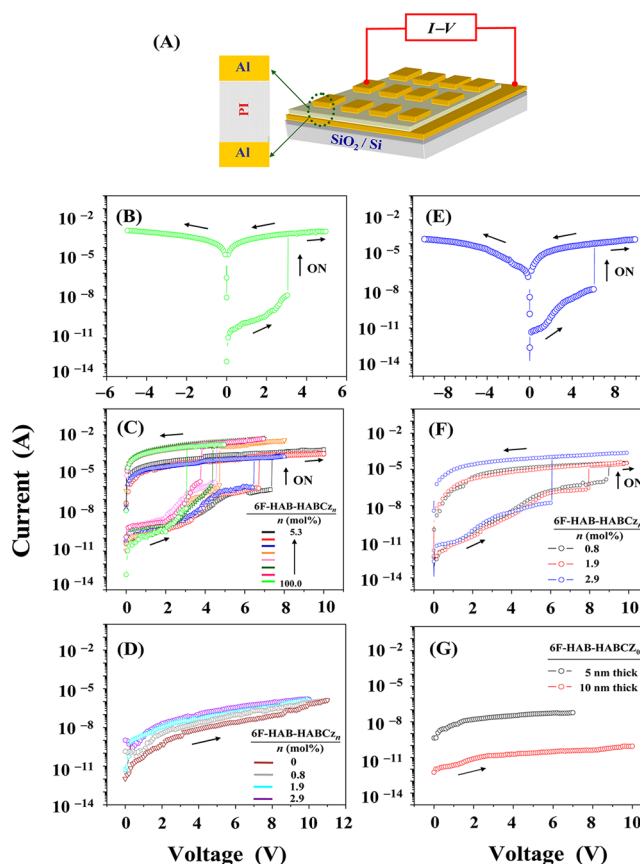
electrodes ($\Phi = -4.20$ eV), the energy barrier for hole injection to the PI layer from the electrode was estimated to be lower than that for electron injection from the electrode to the active layer. Overall, these results indicate that the conduction process in the devices may be predominant with hole injection rather than electron injection.

The above $I-V$ data and analysis results collectively indicate that the observed permanent memory characteristics originated from the carbazole moieties chemically incorporated into the PI polymer, rather than from the other chemical components (trifluoromethyl, imide ring, and hydroxyl groups). The observed permanent memory characteristics were further influenced by the carbazole content as well as the film thickness. The observed carbazole content and film thickness dependencies may be related to the population and distribution of carbazole moieties in the active PI devices. The carbazole population and distribution in each PI device cell can be determined from the chemical composition, GIWAXS and XR analysis results discussed above.

From the chemical composition and the electron density ρ_e of each PI film (Table 1 and Figure 7A), the number of repeat units per unit volume (nm^3) (= N_{ru}), and the number of carbazole moieties per unit volume (= N_{CZ}), were estimated (Table 2). From the N_{CZ} data, the number of carbazole

21697

dx.doi.org/10.1021/am506915n | ACS Appl. Mater. Interfaces 2014, 6, 21692−21701

Table 2. Characteristics of 6F-HAB-HABCZ$_n$ PI thin films

PI film	$n_{HABCZ}{}^a$ (mol %)	$d_{1,\perp}/d_{1,\parallel}{}^b$	$\rho_e{}^c$ (nm^{-3})	$N_{ru}{}^d$ (nm^{-3})	$N_{CZ}{}^e$ (nm^{-3})	$N_{CZ,cell}{}^f$ (20 nm^{-1} × 0.5 × 0.5 mm^{-2})	$\phi_{CZ,cell}{}^g$ (vol %)	$L_{CZ,\perp(i)}{}^h$ (nm)	$L_{CZ,\perp(a)}{}^i$ (nm)	$V_{c,ON}{}^j$ (V) 20 nm thick cell	$V_{c,ON}{}^j$ (V) 12 nm thick cell
6F-HAB-HABCz$_0$	0.0	0.964	461.3 (2.4)^k							^{l}	^{m}
6F-HAB-HABCz$_{0.8}$	0.8	0.967	447.1 (4.7)	1.408	0.0113	5.63 × 10^{10}	0.26	2.514	2.430		8.97
6F-HAB-HABCz$_{1.9}$	1.9	0.965	444.6 (3.1)	1.390	0.0264	1.32 × 10^{11}	0.61	1.927	1.860		7.95
6F-HAB-HABCz$_{2.9}$	2.9	0.965	443.6 (1.9)	1.378	0.0400	2.00 × 10^{11}	0.93	1.699	1.640		6.06
6F-HAB-HABCz$_{5.3}$	5.3	0.967	441.8 (1.5)	1.352	0.0716	3.58 × 10^{11}	1.66	1.443	1.395	7.35	
6F-HAB-HABCz$_{6.9}$	6.9	0.969	440.0 (0.9)	1.333	0.0920	4.60 × 10^{11}	2.13	1.351	1.308	6.70	
6F-HAB-HABCz$_{12.0}$	12.0	0.969	437.5 (1.9)	1.285	0.154	7.71 × 10^{11}	3.57	1.190	1.153	6.46	
6F-HAB-HABCz$_{24.6}$	24.6	0.969	425.8 (5.6)	1.163	0.286	1.43 × 10^{12}	6.63	1.044	1.012	4.72	
6F-HAB-HABCz$_{27.0}$	27.0	0.964	410.9 (1.4)	1.107	0.299	1.49 × 10^{12}	6.93	1.036	0.998	4.55	
6F-HAB-HABCz$_{56.0}$	56.0	0.966	397.8 (2.1)	0.925	0.518	2.59 × 10^{12}	12.00	0.945	0.912	4.35	
6F-HAB-HABCz$_{80.6}$	80.6	0.958	375.4 (3.7)	0.781	0.630	3.15 × 10^{12}	14.59	0.919	0.880	3.80	
6F-HAB-HABCz$_{100}$	100.0	0.958	357.9 (1.7)	0.688	0.688	3.44 × 10^{12}	15.95	0.908	0.870	3.06	

^{a}The mol % of HABCZ unit in 6F-HAB-HABCZ$_n$, which was determined by ^{1}H NMR spectroscopy. ^{b}The anisotropic orientation ratio of PI polymer chains in the PI film where $d_{1,\perp}$ and $d_{1,\parallel}$ are the d-spacings of the scattering peak centered around 11° along the α_f direction (i.e., the out-of-plane direction of the film) and the $2\theta_f$ direction (i.e., the in-plane direction of the film), respectively. ^{c}The electron density of PI film, which was determined by synchrotron X-ray reflectivity analysis. ^{d}The number of repeat units per unit volume (nm^3) in the PI film, which was estimated from the measured ρ_e and chemical composition. ^{e}The number of carbazole moieties per unit volume (nm^3) in the PI film, which was estimated from the measured ρ_e and chemical composition. ^{f}The number of carbazole moieties per device cell (whose dimension is 20 nm (thick) × 0.5 mm × 0.5 mm). ^{g}The volume fraction of carbazole moieties per device cell (whose dimension is 20 nm (thick) × 0.5 mm × 0.5 mm), which was estimated from $N_{CZ,cell}$ and v_{CZ} (the molecular volume of a single carbazole moiety was obtained from the mass density). ^{h}The mean center-to-center distance of carbazole moieties in the device cell, which was estimated from $\phi_{CZ,cell}$ and v_{CZ} under the assumption that the carbazole moieties are distributed homogeneously and isotropically in the PI film layer of the device cell. ^{i}The mean center-to-center distance of carbazole moieties across between the top and bottom electrodes in the PI film layer with a certain degree of anisotropically oriented polymer chains. ^{j}The critical voltage to switch on the device. ^{k}Error extracted over the sweep range ±1.0% of the χ^2 value obtained by best-fitting the XR data with the chosen model, a most proper structural model; thus, this error is different from common standard deviation. The quality of the XR data analysis was achieved with Ω = 1.0−2.6%. $^l V_{c,ON}$ could not be measured because of dielectric characteristics of the PI film. $^m V_{c,ON}$ could not be measured for the PI films with 10 and 5 nm thick.

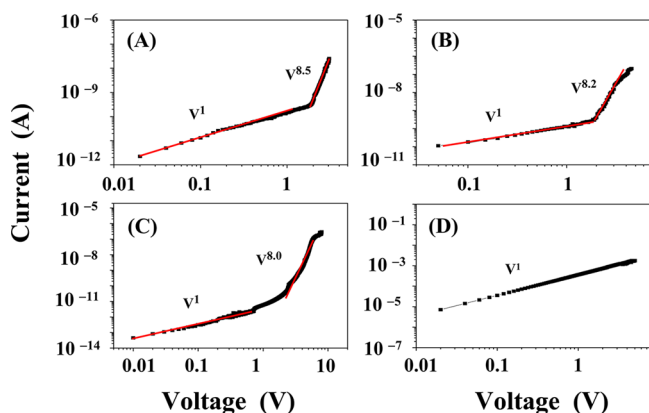**Figure 6.** I−V plots of the Al/PI/Al devices. The OFF-state: (A) 20 nm thick 6F-HAB-HABCBZ$_{100}$ PI film; (B) 20 nm thick 6F-HAB-HABCBZ$_{27.0}$ PI film; (C) 12 nm thick 6F-HAB-HABCBZ$_{1.9}$ PI film. The symbols are the measured data and the solid lines are curves fitted with the ohmic conduction and trap-limited space charge limited current (SCLC) models. The ON-state: (D) 20 nm thick 6F-HAB-HABCBZ$_{100}$ PI film. The symbols are the measured data and the solid lines are curves fitted with the ohmic current model.

moieties per device cell volume (0.5 mm × 0.5 mm × 20 nm) (= $N_{CZ,cell}$) was further estimated. The $N_{CZ,cell}$ value varied in the range of 5.63 × 10^{10} to 3.44 × 10^{12} as the content of HABCZ units in the PI increased from 0.8 mol % to 100 mol % (Table 2 and Figure 7B). The molecular volume of a single carbazole (= v_{CZ}) was estimated to be 0.2317 nm^3 from the mass density of 1.198 g/cm^3 at room temperature.[21,22] From the $N_{CZ,cell}$ and v_{CZ} values, the volume fraction in percent of carbazole moieties per device cell (= $\phi_{CZ,cell}$) was estimated. The $\phi_{CZ,cell}$ value increased from 0.26 vol % to 15.95 vol % as the content of HABCZ unit in the PI increased from 0.8 mol % to 100 mol % (Table 2 and Figure 7C). Assuming that the carbazole moiety is a spherical particle with a radius of r_{CZ} = 0.381 nm (whose volume equals to the v_{CZ} value), and that the carbazole moieties are distributed homogeneously and isotropically in the device cell, the mean center-to-center distance of carbazole moieties in the device cell (= $L_{CZ,\perp(i)}$) was further estimated from the $\phi_{CZ,cell}$ and v_{CZ} values, using a relationship[23]

$$L_{CZ,\perp(i)} = \frac{R_{CZ}\exp(8\phi_{CZ,cell})}{\phi_{CZ,cell}^{1/3}} \cdot \Gamma\left(\frac{4}{3}, 8\phi_{CZ,cell}\right)$$

(4a)

21698

dx.doi.org/10.1021/am506915n | ACS Appl. Mater. Interfaces 2014, 6, 21692−21701
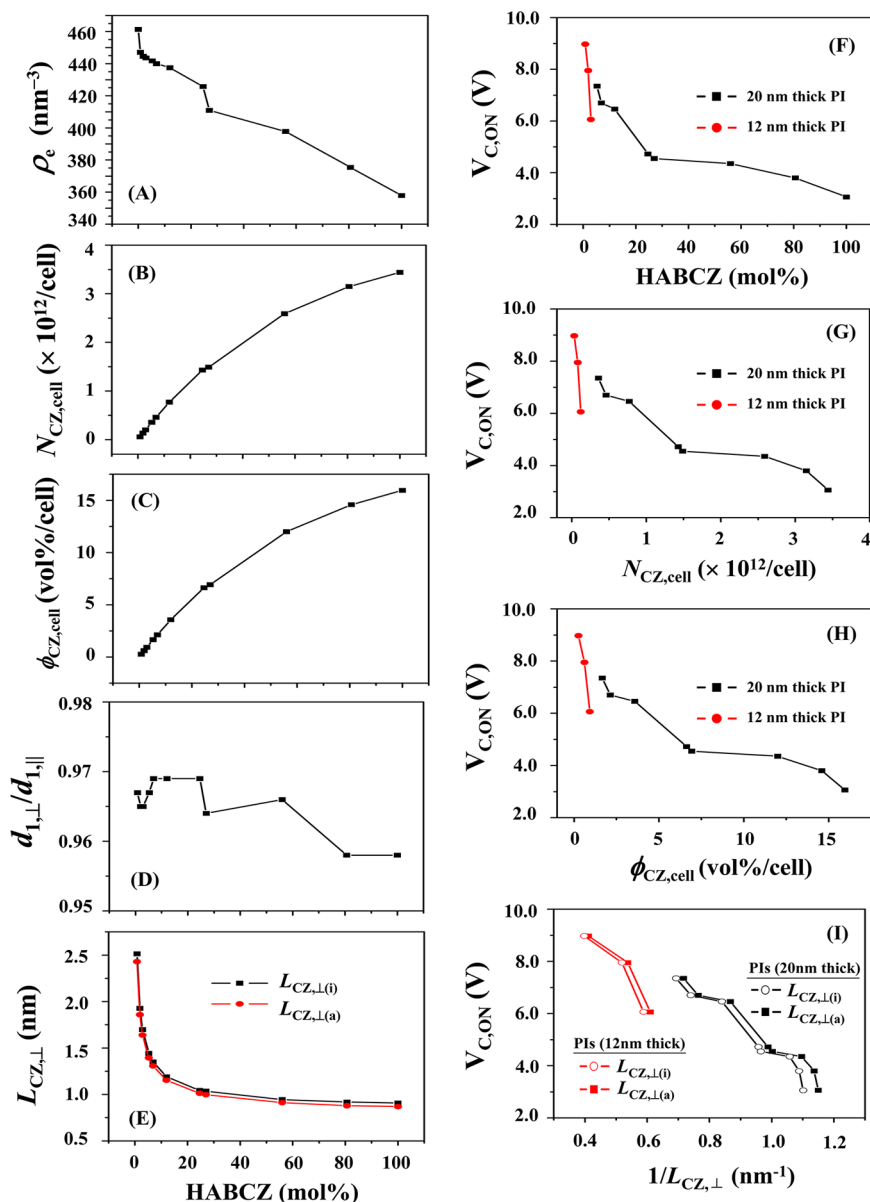
Figure 7. Characteristic parameters of the 6F-HAB-HABCZ$_n$ PI thin films and their correlations to the electrical memory performance: (A) electron density ρ_e variations of the PI film with the HABCZ content; (B) variations in the number of carbazole moieties per device cell (20 nm thick $\times$ (0.5 mm $\times$ 0.5 mm area)) ($N_{CZ,cell}$) with the HABCZ content; (C) variations in the volume fraction of carbazole moiety per device cell (20 nm thick $\times$ (0.5 mm $\times$ 0.5 mm area)) ($\phi_{CZ,cell}$) with the HABCZ content; (D) variations of the anisotropic orientation ratio of the PI chains (which were determined from the scattering peak 1) ($d_{1,\perp}/d_{1,\parallel}$) with the HABCZ content; (E) variations in the mean center-to-center distance of carbazole moieties ($L_{CZ,\perp(a)}$ and $L_{CZ,\perp(i)}$) along the across between the top and bottom electrodes where $L_{CZ,\perp(a)}$ and $L_{CZ,\perp(i)}$ have been determined with and without counting the anisotropic orientation ratio, respectively; (F) variations of the electrical switching-ON voltage $V_{c,ON}$ in the device cell (20 or 12 nm thick PI layer) with the HABCZ content; (G) variations in the $V_{c,ON}$ in the device cell with $N_{CZ,cell}$; (H) variations in the $V_{c,ON}$ in the device cell with $\phi_{CZ,cell}$; (I) variations in the $V_{c,ON}$ in the device cell with $L_{CZ,\perp(a)}$ and $L_{CZ,\perp(i)}$.

$$\Gamma(x,\, a) = \int_a^\infty t^{x-1} \exp(-t)dt \tag{4b}$$

where $\Gamma(x,a)$ is an incomplete Gamma function. The obtained $L_{CZ,\perp(i)}$ values are summarized in Table 2 and Figure 7E. The $L_{CZ,\perp(i)}$ value varied in the range of 2.514 to 0.908 nm as the content of the HABCZ unit in the PI increased from 0.8 mol % to 100 mol %. Considering the anisotropic orientations of the PI chains in the thin films (see the anisotropic ratios $d_{1,\perp}/d_{1,\parallel}$ in Table 1 and Figure 7D), the mean center-to-center distance of carbazole moieties along the z-direction in the device cell (i.e., across the gap between the top and bottom electrodes) (=

$L_{CZ,\perp(a)}$) might be further estimated. The $L_{CZ,\perp(a)}$ value varied in the range of 2.430 to 0.870 nm as the content of the HABCZ unit in the PI increased from 0.8 mol % to 100 mol % (Table 2 and Figure 7E). Overall, for each PI film, the $L_{CZ,\perp(a)}$ value was smaller than the $L_{CZ,\perp(i)}$ value.

The above-determined parameters can be correlated with the electrical switching-ON (i.e., $V_{c,ON}$) of the 6F-HAB-HABCZ$_n$ PI devices, as shown in Figures 7F–I. In addition, the parameters can be further correlated with the ON-current level of the PI devices (Figures 5C and F). First, in case of the 20 nm-thick PI device cell (0.5 mm $\times$ 0.5 mm), electrical switching-ON required at least 3.58×10^{11} carbazole moieties

(= $N_{CZ,cell}$; which corresponded to $\phi_{CZ,cell}$ = 1.66 vol %) or higher; in this regime, lower $N_{CZ,cell}$ values led to a higher $V_{c,ON}$ value and lower ON-current level. Second, the PI device cells with $N_{CZ,cell} < 3.58 \times 10^{11}$ ($\phi_{CZ,cell} < 1.66$ vol %) required a thickness reduction of the PI active layer to switch on, with the 12 nm-thick PI device cells exhibiting electrical switching. In these devices, a lower $N_{CZ,cell}$ value still caused a higher $V_{c,ON}$ value and lower ON-current level. Third, the electrical switching of the 20 nm-thick PI device required a positional distribution of carbazole moieties with $L_{CZ,\perp} \leq$ ca. 1.4 nm ($L_{CZ,\perp(a)} \leq 1.395$ nm and $L_{CZ,\perp(i)} \leq 1.443$ nm) across the top and bottom electrodes; otherwise, the device could not switch on. In this positional distribution regime, a larger $L_{CZ,\perp}$ value caused a higher $V_{c,ON}$ value and lower ON-current level. Finally, in the case of the PI device cells with $L_{CZ,\perp} >$ ca. 1.4 nm, electrical switching-ON required a thickness reduction of the PI active layer. The 12 nm-thick PI device cells with $L_{CZ,\perp} >$ ca. 1.4 nm exhibited electrical switching-ON; in these devices, a larger $L_{CZ,\perp}$ value also caused a higher $V_{c,ON}$ value and lower ON-current level.

The above correlations provide important scientific insights into the electrical memory mechanism in 6F-HAB-HABCZ$_n$ PI devices. The incorporated carbazole moieties play critical roles in the permanent memory characteristics of such devices. The carbazole moieties act as charge trapping sites and are further involved in charge transportation. The electrical switching behavior driven by the carbazole moieties was governed by trap-limited SCLC and ohmic conduction. Considering the nonconjugated backbone characteristics of the PI, charge transportation in these systems occurs by means of a hopping process via the carbazole charge-trap sites. Therefore, the charge transportation is strongly dependent on the population and positional distribution of carbazole moieties in the active PI layer. Moreover, the charge transportation is also significantly affected by the thickness of the active PI layer. Both the electrical switching-ON voltage and the On-current level strongly depended on the population and positional distribution of carbazole moieties as well as on the PI layer thickness. Taking these observations into account, the observed PI layer thickness dependencies of the electrical switching-ON voltage and On-current level can be attributed in part to marginal levels of charge mobility in the PI films.

CONCLUSIONS

A series of carbazole-containing polyimides, 6F-HAB-HABCZ$_n$ PIs, with various compositions were synthesized and their chemical compositions were determined. All of the synthesized PIs were stable to at least 325 °C. Their band gap and HOMO and LUMO levels were found to result mainly from the carbazole moiety. In nanoscale thin films, the PI chains tended to orient in the film plane, but the in-plane orientation level was not high and the in-plane orientational distribution was rather broad. The degree of in-plane orientation was enhanced with increasing the carbazole content. As a result of the in-plane orientation, the PI chains had shorter interdistances along the out-of-plane direction of the film than along the in-plane direction. In addition, the electron density in the nanoscale thin films decreased with increasing content of the relatively bulky carbazole moiety.

The 6F-HAB-HABCZ$_n$ thin film layers in devices with Al electrodes exhibited electrically permanent memory behavior. The memory behavior was found to be governed by trap-limited SCLC and ohmic conduction. Consideration of the

HOMO and LUMO levels of the PIs and the work function of the electrodes suggests that the conduction processes may be dominated by the injection of holes rather than electrons. The electrical switching characteristics observed in the PI devices were found to originate from the incorporated carbazole moieties rather than the other chemical components. Specifically, the carbazole moieties played key roles in charge trapping as well as in charge transportation. However, the electrical memory performance characteristics (e.g., switching voltage and ON-current level) were found to vary with the carbazole content as well as the thickness of the PI film. These dependencies were found to strongly correlate with the population and positional distribution of carbazole moieties in the PI layers, which were extracted from the measured chemical composition, electron density, and anisotropic chain orientation. Considering that the PI backbone is not conjugated, all the measured data and analysis results strongly indicate that the electrical switching-ON (i.e., memory) behavior of the PI thin films arises from the carbazole moieties acting as charge traps and a hopping process using the carbazole charge-trap sites as stepping-stones.

AUTHOR INFORMATION

Corresponding Author
*E-mail: ree@postech.edu. Tel: +82-54-279-2120. Fax: +82-54-279-3399.

Author Contributions
[†]B.J.R., W.K., and K.K. contributed equally to this work.

Notes
The authors declare no competing financial interest.

REFERENCES

(1) Lin, W. P.; Liu, S. J.; Gong, T.; Zhao, Q.; Huang, W. Polymer-Based Resistive Memory Materials and Devices. *Adv. Mater.* **2014**, *26*, 570−606.

(2) Hahm, S. G.; Ko, Y.-G.; Kwon, W.; Ree, M. Programmable Digital Polymer Memories. *Curr. Opin. Chem. Eng.* **2013**, *2*, 79−87.

(3) Kurosawa, T.; Higashihara, T.; Ueda, M. Polyimide Memory: A Pithy Guideline for Future Applications. *Polym. Chem.* **2013**, *4*, 16−30.

(4) Ling, Q. D.; Liaw, D. J.; Zhu, C.; Chan, D. S. H.; Kang, E. T.; Neoh, K. G. Polymer Electronic Memories: Materials, Devices and Mechanisms. *Prog. Polym. Sci.* **2008**, *33*, 917−978.

(5) Hahm, S. G.; Choi, S.; Hong, S.-H.; Lee, T. J.; Park, S.; Kim, D. M.; Kwon, W.-S.; Kim, K.; Kim, O.; Ree, M. Novel Rewritable, Non-volatile Memory Devices Based on Thermally and Dimensionally Stable Polyimide Thin Films. *Adv. Funct. Mater.* **2008**, *18*, 3276−3282.

(6) Tian, G.; Wu, D.; Qi, S.; Wu, Z.; Wang, X. Dynamic Random Access Memory Effect and Memory Device Derived from a Functional Polyimide Containing Electron Donor-Acceptor Pairs in the Main Chain. *Macromol. Rapid Commun.* **2011**, *32*, 384−389.

(7) Hu, B.; Zhuge, F.; Zhu, X.; Peng, S.; Chen, X.; Pan, L.; Yan, Q.; Li, R. W. Nonvolatile Bistable Resistive Switching in a New Polyimide

Bearing 9-Phenyl-9H-carbazole Pendant. *J. Mater. Chem.* **2012**, *22*, 520−526.

(8) Li, Y. Q.; Fang, R. C.; Zheng, A. M.; Chu, Y. Y.; Tao, X.; Xu, H. H.; Ding, S. J.; Shen, Y. Z. Nonvolatile Memory Devices Based on Polyimides Bearing Noncoplanar Twisted Biphenyl Units Containing Carbazole and Triphenylamine Side-chain groups. *J. Mater. Chem.* **2011**, *21*, 15643−15654.

(9) Li, Y.; Fang, R.; Ding, S.; Shen, Y. Rewritable and Non-Volatile Memory Effects Based on Polyimides Containing Pendant Carbazole and Triphenylamine Groups. *Macromol. Chem. Phys.* **2011**, *212*, 2360−2370.

(10) Shi, L.; Tian, G.; Ye, H.; Qi, S.; Wu, D. Volatile Static Random Access Memory Behavior of an Aromatic Polyimide Bearing Carbazole-tethered Triphenylamine Moieties. *Polymer* **2014**, *55*, 1150−1159.

(11) Lee, S. W.; Kim, S. I.; Lee, B.; Choi, W.; Chae, B.; Kim, S. B.; Ree, M. Photoreactions and Photoinduced Molecular Orientations of Films of a Photoreactive Polyimide and Their Alignment of Liquid Crystals. *Macromolecules* **2003**, *36*, 6527−6536.

(12) Park, S.; Kim, K.; Kim, J. C.; Kwon, W.; Kim, D. M.; Ree, M. Synthesis and Nonvolatile Memory Characteristics of Thermally, Dimensionally and Chemically Stable Polyimides. *Polymer* **2011**, *52*, 2170−2179.

(13) Yoon, J.; Kim, K.-W.; Kim, J.; Heo, K.; Jin, K. S.; Jin, S.; Shin, T. J.; Lee, B.; Rho, Y.; Ahn, B.; Ree, M. Small-Angle X-ray Scattering Station 4C2 BL of Pohang Accelerator Laboratory for Advance in Korean Polymer Science. *Macromol. Res.* **2008**, *16*, 575−585.

(14) Lee, B.; Park, Y.-H.; Hwang, Y.; Oh, W.; Yoon, J.; Ree, M. Ultralow-k Nanoporous Organosilicate Dielectric Films Imprinted with Dendritic Spheres. *Nat. Mater.* **2005**, *4*, 147−150.

(15) Yoon, J.; Lee, S. W.; Choi, S.; Heo, K.; Jin, K. S.; Jin, S.; Kim, G.; Kim, J.; Kim, K.-W.; Kim, H.; Ree, M. Two-Dimensionally Well-Ordered Multilayer Structures in Thin Films of a Brush Polypeptide. *J. Phys. Chem. B* **2008**, *112*, 5338−5349.

(16) Park, B.-J.; Rah, S.-Y.; Park, Y.-J.; Lee, K.-B. PLS Bending Magnet X-Ray Beamline 3C2. *Rev. Sci. Instrum.* **1995**, *66*, 1722−1724.

(17) Bolze, J.; Kim, J.; Huang, J.-Y.; Rah, S.; Youn, H. S.; Lee, B.; Shin, T. J.; Ree, M. Current Status of the Synchrotron Small-Angle X-Ray Scattering Station BL4C1 at the Pohang Light Source. *Macromol. Res.* **2002**, *10*, 2−12.

(18) Yoon, J.; Jin, K. S.; Kim, H. C.; Kim, G.; Heo, K.; Jin, S.; Kim, J.; Kim, K.-W.; Ree, M. Quantitative Analysis of Lamellar Structures in Brush Polymer Thin Films by Synchrotron Grazing Incidence X-Ray Scattering. *J. Appl. Crystallogr.* **2007**, *40*, 476−488.

(19) Parratt, L. G. Surface Studies of Solids by Total Reflection of X-Rays. *Phys. Rev.* **1954**, *95*, 359−369.

(20) Braun, D. Electronic Injection and Conduction Processes for Polymer Devices. *J. Polym. Sci. Part A: Polym. Phys.* **2003**, *41*, 2622−2629.

(21) Das, A.; Frenkel, M.; Gadalla, N. A. M.; Kudchadker, S.; Marsh, K. N.; Rodgers, A. S.; Wilhoit, R. C. Thermodynamic and Thermophysical Properties of Organic Nitrogen Compounds. Part II. 1- and 2-Butanamine, 2-Methyl-1-Propanamine, 2-Methyl-2-Propanamine, Pyrrole, 1-, 2-, and 3-Methylpyrrole, Pyridine, 2-, 3-, and 4-Methylpyridine, Pyrrolidine, Piperidine, Indole, Quinoline, Isoquinoline, Acridine, Carbazole, Phenanthridine, 1- and 2-Naphthalenamine, and 9-Methylcarbazole. *J. Phys. Chem. Ref. Data* **1993**, *22*, 659−782.

(22) Lide, D. R. *CRC Handbook of Chemistry and Physics*, 88th ed; CRC: New York, 2007; pp 3−86.

(23) Bansal, P. P.; Ardell, A. J. Average Nearest-Neighbor Distances between Uniformly Distributed Finite Particles. *Metallography* **1972**, *5*, 97−111.